Article

Numerical Simulation and Analysis of the Airflow Field in the Crushing Chamber of the Hammer Mill

Hongcheng Li, Shanchen Jiang, Rong Zeng, Jie Geng, and Zhiyou Niu*
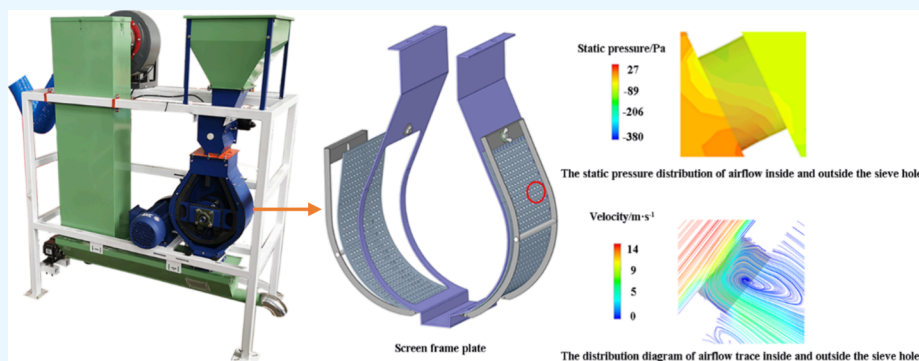
Read Online

ACCESS | 📊 Metrics & More | 📰 Article Recommendations

Static pressure/Pa

The static pressure distribution of airflow inside and outside the sieve hole

Velocity/m·s⁻¹

Screen frame plate

The distribution diagram of airflow trace inside and outside the sieve hole

ABSTRACT: The airflow dynamics within hammer mills' crushing chambers significantly affect material crushing and screening. Understanding the crushing mechanism necessitates studying the airflow distribution. Using a self-built crushing test platform and computational fluid dynamics (CFD) simulations, we investigated the impact of screen aperture size, rotor speed, hammer-screen clearance, hammer quantity, and mass flow rate on airflow distribution within the rotor region, circulation layer, and screen apertures. Results indicated generally uniform axial static pressure distribution within the rotor region, with radial gradients. Increased rotor speed improved radial static pressure gradients, while higher mass flow rates reduced them. The highest airflow velocity within the circulation layer reached approximately 83.46% of the hammer tip's tangential velocity. Greater rotor speed and hammer quantity intensified circulation airflow, whereas increased mass flow rate decreased it. Eddies formed within screen apertures with higher rotor speeds and hammer quantities but diminished with larger apertures and higher mass flow rates. Static pressure differences across screen apertures increased with mass flow rate and rotor speed but decreased significantly with larger apertures. This systematic examination provides insights into airflow distribution within hammer mill crushing chambers, offering a theoretical foundation for improving and designing hammer mills.

1. INTRODUCTION

Crushing powdered materials is one of the important processes in the production of feed.[1,2] After being crushed, the materials are turned into powder, which not only makes the feed processing stable and efficient but also improves the conversion rate of nutrients and the productivity of the animals.[3] Hammer mills are often used in the crushing process which are easy to operate, wide to use, and low cost.[4,5] However, the hammer mill may consume more energy than crushing devices such as ball mills and counter roll mills, and there are some problems like overcrushing and temperature rising of material in the crushing process.[6,7] Liu et al. studied that the airflow distribution in the crushing chamber, material properties, crusher design, and operational parameters were all related to the high energy consumption of hammer mills.[8] Among them, the airflow field in the crushing chamber is one of the most important elements affecting the performance of hammer mills, which could cause particle movement and affect the ability of mills.[9] Therefore, to

improve the crushing performance, it is essential to investigate the characteristics of airflow distribution in the crushing chamber.

The operation of the hammer mill may be separated into two stages: powder materials crushing and particle screening. There are two processes of crushing powdered materials, including impact crushing and friction crushing. The movement of the particles is influenced by the airflow in the crushing chamber, which affects the impact strength and frequency of the particles' impact with the hammer, the liner, and the screen. In addition,
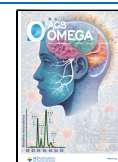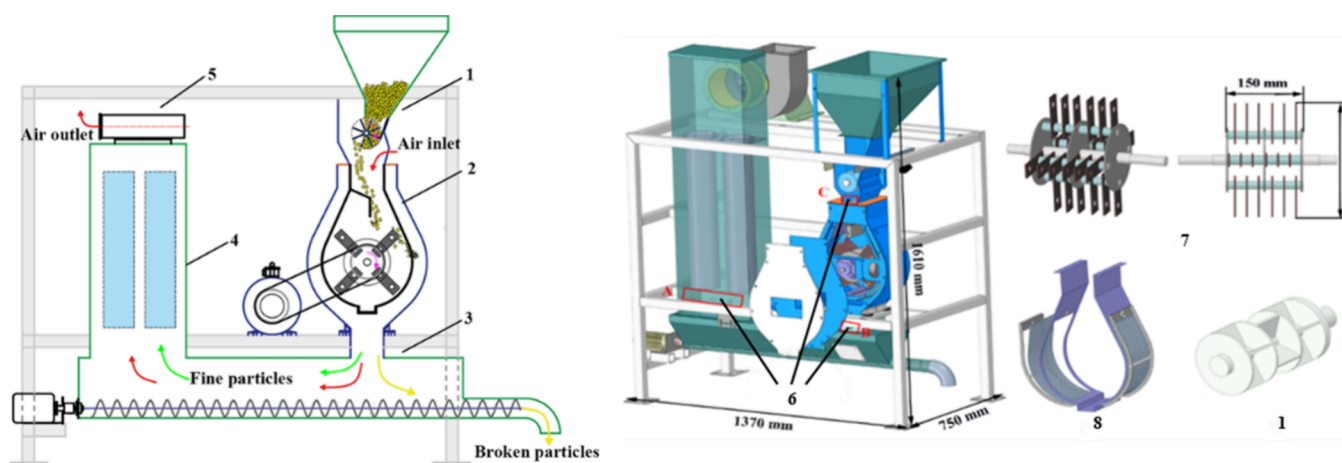
Figure 1. Group of hammer mills. (a) Schematic diagram. (b) Structural diagram.

the drag force of the airflow affects the friction force and impact frequency of particle−particle and particle-screen, which would affect the crushing efficiency when the circulation movement of particles occurs in the circulation layer of the chamber.[10,11] In the process of particles out of the screen, the particles are affected by the action of centrifugal inertia force, airflow drag force, and pressure difference inside and outside the screen apertures. So, the amount of particles screened is influenced by the airflow in the circulation layer, inside and outside the screen aperture.[12−15] Meanwhile, researchers have proposed that the hammer mill should be equipped with a mass flow rate fan to work at the same time, which could change the airflow distribution in the crushing chamber, improving the efficiency of crushing and screening, and reducing overcrushing and temperature rising. Therefore, the hammer mills could crush efficiently, and uniformity of particle size distribution of crushed materials, and reduce energy consumption.[1,16]

To determine the appropriate mass flow rate and other operating parameters of hammer mills, researchers have extensively studied the airflow distribution in the crushing chamber. The results showed a distinct stratification and gradient distribution along the radial direction of the rotor in the static pressure within the crushing chamber, but there were few differences in the static pressure and velocity in the axial direction. From the tip of the hammer to the center of the rotor, the static pressure steadily decreased, with the biggest negative pressure value in the center of the rotor.[9,17−21] The airflow in the crushing chamber moves annularly with the rotor, and the airflow velocity gradually increases from the center of the rotor along the radial direction and reaches the maximum at the tip of the hammer. The airflow near the screen surface forms a high-speed and high-pressure circulation airflow (airflow circulation layer) with the high-speed rotating hammer. The drag force of the airflow circulation layer on the particles is beneficial to the friction crushing between the particles, but the airflow circulation layer also causes the material to condense into the rotor's center and precludes screening.[9] The static pressure of the airflow field and the velocity of the circulation layer in the crushing chamber increase with the increase of the rotor speed.[22] The mass flow rate and the fan effect of the rotor raise the static pressure difference between the interior and outside of the screen apertures, which improves the efficiency of screening particles. However, if the static pressure differential is too significant, large particles will be adsorbed and block the screen apertures, reducing the efficacy of screening broken particles. In

conclusion, the overall airflow field distribution of hammer mills has been extensively studied, but few people have systematically analyzed the influence of the operating parameters of the mill on the airflow field of the mill. In particular, the a lack of research on the distribution characteristics and influencing factors of the airflow field inside and outside the circulation layer and the screen in the crushing room.

This study examined the airflow distribution of the rotor region, circulation layer, inside and outside the screen apertures in the crushing chamber by using the CFD solver (Fluent 2019 R2). It also studied the influences of screen aperture size, rotor speed, hammer-screen clearance, hammer number, and mass flow rate on the airflow distribution in the crushing chamber. This study is expected to improve the research on the airflow distribution in the crushing chamber, and provide a theoretical basis for examining the crushing mechanism, provide a reference for the setting of the working parameters of the hammer mills.

2. EXPERIMENTS

2.1. Experimental Setup. The study of airflow was carried out with a self-built hammer mill group shown in Figure 1. It included an impeller-feeder, a hammer mill, a screw, a bag filter, and a mass flow rate fan. The actual hammer mill was made up of a high-speed spinning rotor with 24 hammers that were 30 × 90 × 3 mm, a crushing chamber that was 160 mm deep, and a screen with a packing angle of 300°. Feed raw materials entered the crushing chamber independently during the crushing operation through the impeller feeder. They were originally shattered by the high-speed rotating hammer before being struck by the airflow and coming into touch with the screen. The particles bounce back after an impact on the screen. In this way they were constantly being struck by the hammer and the screen, getting smaller and smaller until they finally flew out of the screen apertures. The large particles that were remaining in the crushing chamber were further crushed by the friction force of particle−particle and particle-screen and the impact force of particle-hammer and particle-screen, and particles were discharged through the screen apertures until the particle size was approved.[15] The bag filter adsorbed the fine particles after the crushed material particles were screwed into the aggregate box, reducing the amount of dust that was released. The maximum suction capacity of the negative pressure fan was 1200 m³/h, but after going through the bag filter, the suction lost air volume. To determine the actual mass flow rate via the crushing chamber, the airflow velocity detection port needed to be located at the

Table 1. Levels of Experimental Factors

Factors	Threshold value	Levels
Screen aperture size/mm	3−6	3, 4, 5 and 6
Rotor speed/rpm	1500−3600[16]	1500, 2200, 2900 and 3600
Hammer-screen clearance/mm	6−18[10,16]	6, 10, 14 and 18
Hammer number	8−32[16]	8, 16, 24 and 32
Mass flow rate/kg·h^{-1}	0.01−0.21[16]	0.01, 0.10, 0.14 and 0.21

square pipe connecting the bag filter and the winch, as shown in Port A (Figure 1b). Port C and Port B were installed to detect static pressure of airflow at the hammer mill's inlet and outlet to validate the accuracy of the airflow field simulation model (Figure 1b).

2.2. Experimental Design. Cao et al. studied that the aperture type and opening rate of the screen accounted for 33.5%, the hammer tip linear velocity accounted for 31.5%, the hammer screen clearance accounted for 10%, the hammer density accounted for 15%, and the mass flow rate accounted for 10% among the factors affecting the efficiency of the hammer mill.[16] Therefore, to study the factors on the distribution of airflow field in the crushing chamber, screen aperture size, rotor speed, hammer-screen clearance, hammer number, and mass flow rate were chosen as experimental factors for the single-factor simulations. The hammer mill's standard operating settings were as follows: the number of hammers was 24, which are positioned symmetrically, the screen aperture was 4 mm, the rotation speed was 2900 rpm, the hammer-screen clearance was 10 mm, and the mass flow rate was 300 m^3/h. According to the study and the standard parameters setting of the hammer mill, the experimental design was carried out as shown in Table 1.

3. NUMERICAL MODELING

3.1. Mathematical Model. The simulation and analysis of the hammer mill's airflow field revealed that the high-speed rotating hammer's turbulent motion could be present in the airflow field of the crushing chamber.[22] The maximum airflow velocity in the crushing chamber was less than the hammer tip linear velocity v_h.[9,18] The hammer tip linear velocity can be calculated by equation 1.

$$v_h = \omega r \tag{1}$$

where ω and r are the rotational speed of the rotor (r/min) and the rotor radius (mm), respectively.

The maximum rotational speed of the rotor was 3600 r/min and the diameter of the rotor was 300 mm. So, the maximum hammer tip linear velocity was 56.52 m/s, and the maximum velocity of airflow in the crushing chamber was less than 56.52 m/s.

The Mach number (M_a) is widely used in aerodynamics, which is the ratio of velocity to sound velocity and could be calculated by equation 2. Therefore, the maximum M_a of the airflow filed in the chamber was 0.17. When M_a is less than 0.3, the airflow is incompressible.[23]

$$M_a = \frac{v}{a} \tag{2}$$

where M_a is the Mach number, v is the airflow velocity (m/s), and a is the sound velocity.

In the research, the standard k-ε turbulent model is frequently used to solve the simulation motion of fluid turbulent motion. The quantitative variables are turbulent kinetic energy k and

dissipation rate ε, and the model can quantify the turbulence in terms of both airflow and time scales. Based on the solution of the N−S equation, a new transport equation is introduced for these two variables. Consequently, this model is widely utilized in simulation analysis of the hammer mill's airflow field.[24,25] The continuity equation, Reynolds-averaged Navier−Stokes (RANS), energy equation, and ideal gas state equation are all solved by the model to determine the airflow. The governing equations of continuity, RANS equation, energy, and state of the ideal gas are as follows.

Equation of continuity:

$$\frac{\partial}{\partial t}\rho + \nabla(\rho U) = 0 \tag{3}$$

RANS equation:

$$\frac{\partial(\rho U)}{\partial t} + \nabla(\rho U U)$$
$$= -\nabla p + \nabla[\mu(\nabla U) + (\nabla U)^T] + \rho g - \nabla\left[\frac{2}{3}\mu\delta(\nabla U)\right]$$
$$- \nabla(\overline{\rho U'U'}) \tag{4}$$

Equation of energy:

$$\frac{\partial}{\partial t}\left(\frac{1}{2}\rho U^2 + \rho E_i\right) + \nabla(\rho E_i) + \nabla\left(\frac{1}{2}\rho U^2 + \rho E_i\right)U$$
$$= -\nabla p U + k_{eff}\nabla^2 T - \rho(U\nabla|g|h) \tag{5}$$

Equation of state of the ideal gas:

$$\rho = \frac{p_0 + p}{(R_m/M_w)T} \tag{6}$$

where ρ is the fluid density of 1.225 kg/m^3, U is the fluid velocity (m/s), U' is the fluctuating velocity of the fluid (m/s), p is the fluid pressure (Pa), μ is the fluid viscosity of 1.79 e^{-5} kg/m, g is gravity acceleration, δ is the Kronecker delta, E_i is the internal energy of fluid (J/kg), K_{eff} is the effective thermal conductivity of fluid (W/(m·°C)), T is the fluid temperature (K), h is the height from the reference plane (mm), P_0 is the standard pressure (Pa), R_m is the molar gas constant (J/(mol·K)), M_w is the molar weight of the fluid (kg/mol).

In the RANS equation, during the Reynolds average, the Reynolds stress produced an unknowable Reynolds stress term, $\overline{-\rho U'U'}$. To make the equation sealed and solve the airflow velocity, $\overline{-\rho U'U'}$ needs to be represented by the known quantities, which could be calculated by the Boussinesq method[26] as the equation 7.

$$\overline{-\rho U'U'} = \mu_t(\nabla U + (\nabla U)^T) - \frac{2}{3}\mu_t\delta(\nabla U) - \frac{2}{3}\rho k\delta \tag{7}$$
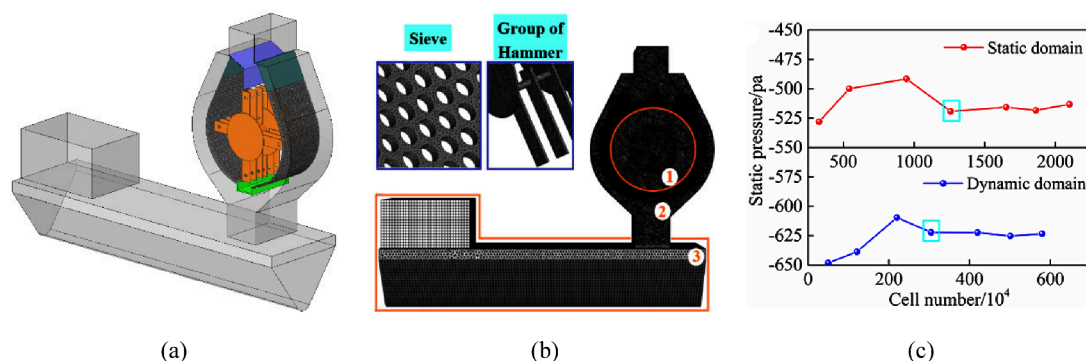
(a)   (b)   (c)

Figure 2. Actual appearance and fluid grids of the hammer mill. (a) Simulation model of the hammer mill. (b) Fluid grids of the hammer mill. (c) Grid independence verification.

Table 2. Mesh Information of the Hammer Mill

Region	Elements	Element Quality		Orthogonal Quality		Skewness	
		Min	Average	Min	Average	Max	Average
1	12603120	0.40	0.83	0.36	0.76	0.64	0.24
2	3068619	0.46	0.82	0.40	0.75	0.60	0.25
3	157865	0.42	0.94	0.45	0.91	0.33	0.11
Value	15848634	0.40	0.83	0.36	0.76	0.64	0.24

where μ_t is the eddy viscosity coefficient, k is the turbulent kinetic energy (m^2/s^2). The correlations between μ_t, k, and ε can be described by eqs 8−10, respectively.

$$\mu_t = \rho C_\mu \frac{k^2}{\varepsilon} \tag{8}$$

$$\frac{\partial}{\partial t}(\rho k) + \frac{\partial}{\partial x_j}(\rho k u_j)$$
$$= \frac{\partial}{\partial x_j}\left[\left(\mu + \frac{\mu_t}{\delta_k}\right)\frac{\partial k}{\partial x_j}\right] + G_k + G_b + \rho\varepsilon + Y_m \tag{9}$$

$$\frac{\partial}{\partial t}(\rho\varepsilon) + \frac{\partial}{\partial x_j}(\rho\varepsilon u_j)$$
$$= \frac{\partial}{\partial x_j}\left[\left(\mu + \frac{\mu_t}{\delta_\varepsilon}\right)\frac{\partial\varepsilon}{\partial x_j}\right] + \rho C_1\varepsilon + \rho C_2\frac{\varepsilon^2}{k + \sqrt{\nu\varepsilon}}$$
$$+ C_{1\varepsilon}\frac{\varepsilon}{k}C_{3\varepsilon}G_b \tag{10}$$

where G_k and G_b are the generation of turbulent kinetic energy due to the mean velocity gradients and buoyancy (m^2/s^2), respectively. Y_m is the contribution of the fluctuating dilatation in compressible turbulence to the overall dissipation rate, ν is the kinematic viscosity (m^2/s), x_j and μ_j are the fluid lengths (mm), and fluid velocity (m/s) to the direction of j, respectively. C_2 and $C_{1\varepsilon}$ are constants. σ_k and σ_ε are turbulent Prandtl Numbers for k and ε, respectively. C_1, $C_{3\varepsilon}$, and S can be calculated as the following equations:

$$C_1 = \max\left[0.43, \frac{\eta}{\eta + 5}\right]$$

$$\eta = S\frac{k}{\varepsilon}$$

$$S = \sqrt{2S_{ij}S_{ji}}$$

$$S_{ij} = \frac{1}{2}\left(\frac{\partial u_j}{\partial u_i} + \frac{\partial u_i}{\partial u_j}\right)$$

$$C_{3\varepsilon} = \tanh\left|\frac{u_{hg}}{u_{vg}}\right| \tag{11}$$

where μ_{hg} and u_{vg} are horizontal and vertical fluid velocities (m/s), respectively. x_i and u_i are the fluid length and fluid velocity to the direction of i, respectively. These parameters were chosen for this investigation under Tsan-Hsing et al.'s study.[26]

3.2. Boundary Conditions and Parameters Setting. The hammer mill's real construction is the basis for building the simulation model. Since the mesh aperture, rotor speed, number of hammers, hammer-sieve clearance, and mass flow rate in the hammer-type crushing unit directly affect the airflow field distribution in the crusher, the simplified simulation model is shown in Figure 2a. The grid of the hammer mill was divided by Ansys Meshing 2019 R2 software shown in Figure 2b. The sweep meshing method was used to split the hexahedral meshes of the bag filter and screw (screw's bottom) (Region 3 in Figure 2b). In Table 2, the mesh quality, mesh orthogonal quality, and mesh skewness of Region 3 all met the simulating requirements.[27] Since the airflow field near the crushing chamber, screen and rotor was the main focus of this work, checking the independence of the rotor and crushing chamber grids was important to ensure the accuracy and stability of the numerical simulation. The static pressure of 1/2 rotor diameter and one point between the two hammers as the reference variables to demonstrate the independence of the dynamic domain grid

(Region 1 in Figure 2b), the static pressure of the screen aperture's center point as the reference variables to demonstrate the independence of the static domain (Region 2 in Figure 2b). The static pressure at the two reference positions stabilized when the dynamic mesh reached 30.6 million and the static mesh exceeded 112.6 million shown in Figure 2c. The airflow field distribution was independent of the grid size since the static pressure at the reference locations virtually remained constant as the number of grids increased. There were 3068619 dynamic domain grids and 12603120 static domain grids in the crushing chamber. The mesh quality, mesh orthogonal quality, and mesh skewness of Regions 1 and 2 all met the simulation requirements shown in Table 2.[27]

The Multiple Reference Frame (MRF) model adopts the calculation model of steady-state approximation. The circular motion is set in the dynamic domain, and the interface between the dynamic domain and the static domain is set as the interface boundary type, which is used to transmit the information difference between the two sides of the interface.[27] The airflow field simulations of classifier mills[28,29] and hammer mills,[30−32] have currently been completed with the MRF model, and the results were accurate and trustworthy. In addition, compared to the sliding mesh model and others, it could reduce the amount of calculation.[33] Therefore, the MRF was applied to simulate the hammer mill. The hammer mill's outlet was set as a mass-flow-outlet, the airflow direction was perpendicular to the boundary surface, and velocity distribution was uniform. The inlet was set as a pressure inlet with 0 Pa because the pressure at the inlet of the hammer mill is nearly equal to the standard atmospheric pressure. The numerical values were set based on the measured value. Due to the fact Ma in the crushing chamber was approximately 0.17, in the range of 0−3, the pressure-based solver (PBS) was appropriate for airflow fluid and used in this research. In the meanwhile, the Coupled algorithm was adopted because of the advances in solving the incompressible flow of rotating motion.[27]

3.3. Analysis. Based on the research on the process of particle crushing and discharging in the hammer mill, the airflow field can be divided into three regions for simulation analysis as shown in Figure 3. Region I represents the static pressure distribution of the airflow field in the rotor diameter range, where small particles become adhered to the rotor center, making it challenging to filter them out.[16] Region II was made up of the circulation layer region along the screen surface, where particles were moved over the screen surface by the airfield drag
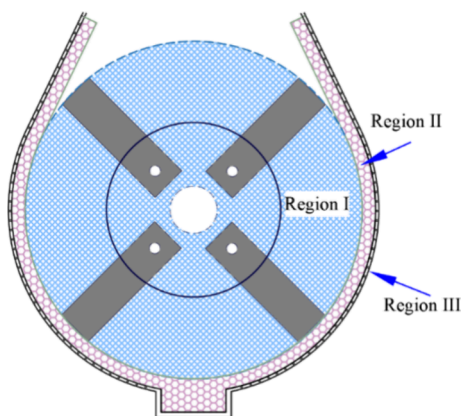
force, and reduced the relative velocity between the hammers and the particles, making it difficult for the particles to be impact-crushed. The particle motion velocity in the circulation layer also affects the screening of particles.[11] Region III was within the screen aperture in the crushing chamber, where the particle screening was impacted by the airflow distribution and trajectory through the screen apertures, as well as by the pressure difference between the inside and outside of the screen aperture.[34] Therefore, the static pressure distribution of the airflow field in Region I, the velocity distribution in Region II, the airflow trajectory through the screen in Region III, and the static pressure difference inside and outside the screen aperture were studied in this work.

4. RESULTS AND DISCUSSION

4.1. Validation of Simulation Model. To measure the accuracy of the simulation, the overall pressure drop between the inlet and outlet in the hammer mill was compared with the results of experiments and numerical simulations shown in Figure 4 at constant screen aperture size (4 mm), constant rotor
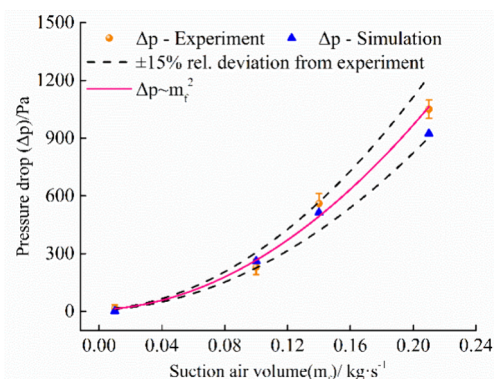
Figure 4. Pressure drop comparison of experiments and numerical simulation.

speed (2900 rpm), and varying mass flow rate. The results show that the pressure drop between the inlet and outlet in the simulation is consistent with experiments. Additionally, there was a 15% or lower difference between simulations and experiments, indicating that the simulation was credible.[29] This method could be applied to simulate the distribution of the airflow field in the hammer mill.

4.2. Static Pressure Distribution in Region I. To study the characteristics of the static pressure distribution, Section 1 and Section 2 were created in Region I shown in Figure 5a. Section 2 was used to analyze the static pressure distribution close to the hammer, and Section 2 was used to analyze the overall static pressure distribution in Region I. The static pressure distribution in Region I is shown in Figure 5b. With characteristics of clear stratification and gradient distribution along the radial direction of the rotor, the fluid static pressure was uniformly distributed along the axial direction and gradually increased along the radial direction away from the center of the rotor. Due to the gradient distribution properties of static pressure in the radial direction, fine particles would move to the center of the rotor under the static gradient force, which increased the residence time of the particles in the crushing chamber, decreased particle screening effectiveness, and led to over grinding, which not only increased the energy consumption but also reduced the efficiency.[35] In Region I, the static pressure

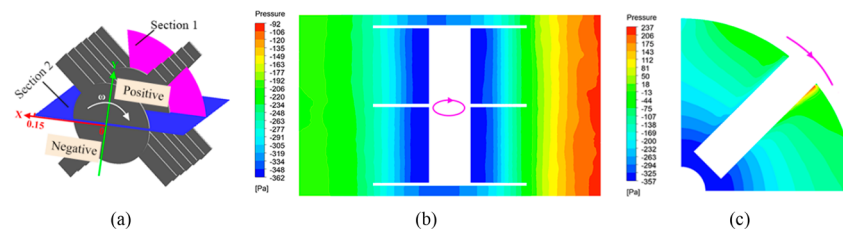**Figure 3.** Schematic diagram of the partition in the crushing chamber.

Figure 5. Static pressure distribution in Region I (normal condition). (a) The diagram of sections. (b) The static pressure of Section 1. (c) The static pressure of Section 2.
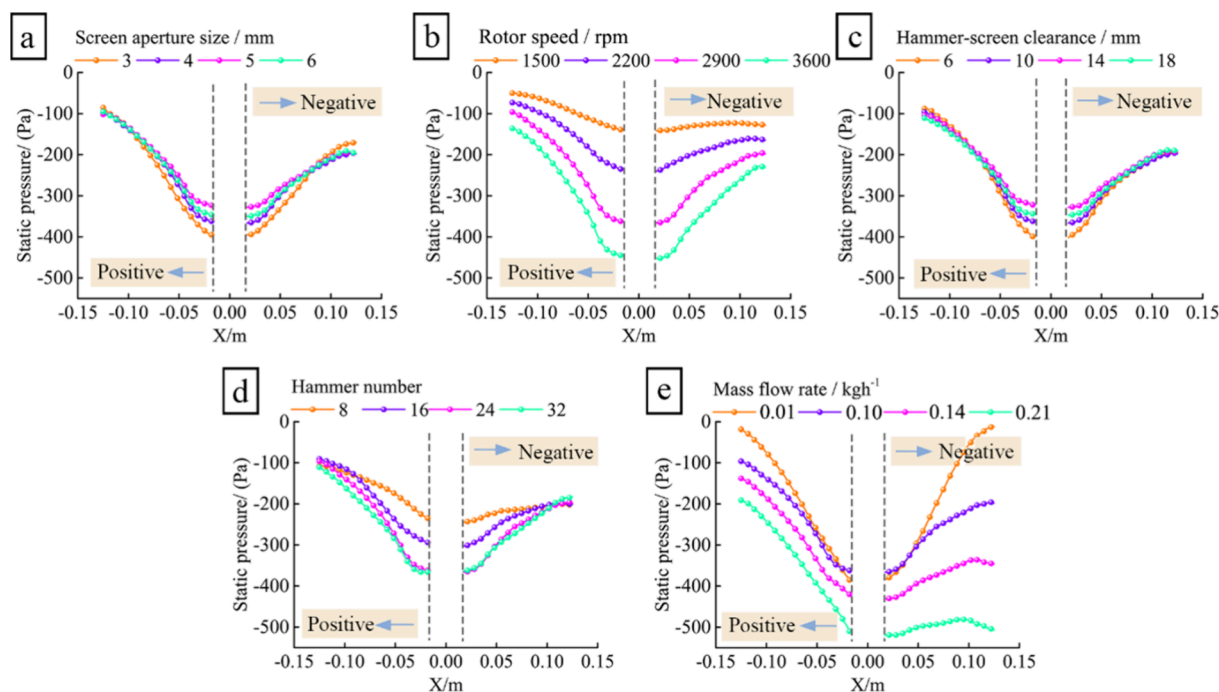

Figure 6. Variation of static pressure with various factors in Region I. (a) Screen aperture size. (b) Rotor speed. (c) Hammer-screen clearance. (d) Hammer number. (e) Mass flow rate.

was higher in the region where the rotor was rotating in a positive direction than it was in the opposite direction. This is because the effect of the hammer on the extrusion force of the airflow in the positive region was stronger than that in the negative region. Therefore, the mechanical energy of airflow increased in the positive region more than it did in the negative region, which caused substantial thermal motion of gas molecules. Moreover, since the static pressure of airflow was mostly produced by the thermal motion of molecules, the static pressure in the positive region was higher than that in the negative region.[36] Due to the large extrusion pressure of the high-speed rotating hammer in the crushing chamber, a high-pressure region was formed at the tip of the hammer, and the static pressure value of the airflow at the tip of the hammer is the largest, which was similar to the research of Hirohisa Takeuchi and Yang Kang.[17,37] During extrusion, the mechanical energy of the airflow in the region increased to its peak, leading to the strongest thermal movement of gas molecules and the highest static pressure in the region.

Figure 6 shows the effects of screen aperture size, rotor speed, hammer-screen clearance, hammer number, and mass flow rate on the static pressure distribution of the airflow field in Region I. The static pressure increased as the screen aperture and hammer-screen clearance increased, when screen aperture and hammer-screen clearance were in the range of 2−5 mm and 6−

14 mm respectively, (Figures 6a and Figure 6c). However, the static pressure with a screen aperture of 5 mm was higher than 6 mm, and the static pressure with a hammer-screen clearance of 14 mm was higher than 18 mm. The static pressure decreased as the rotor speed, hammer number, and mass flow rate increased (Figure 6b, Figure 6d, and Figure 6e).

The static pressure gradient force along the radial direction of the airflow field caused the fine particles to move to the center of the rotor. However, the static pressure varied due to changes in various factors, and it was a challenge to analyze these factors' influence on the static pressure gradient. Therefore, to study the impact of various factors on the static pressure gradient, the radial static pressure of the airflow field was normalized. The ratio of the static pressure value (P_s) at each point and the maximum static pressure (P_{max}) in the radial direction of the airflow was used as the normalization results shown in Figure 7. The static pressure gradient of the positive region was higher than that of the negative region. The slope of the fitting line indicated the change rate of the static pressure gradient, that is, the larger the absolute value of the slope, the greater the static pressure gradient. The larger the static pressure gradient force absorbed by the particles, the more particles move to the rotor center, and the less efficient the particle screening. The static pressure gradient reduced as screen aperture size, hammer-screen clearance, and mass flow rate increased (Figures 7a, 7c,
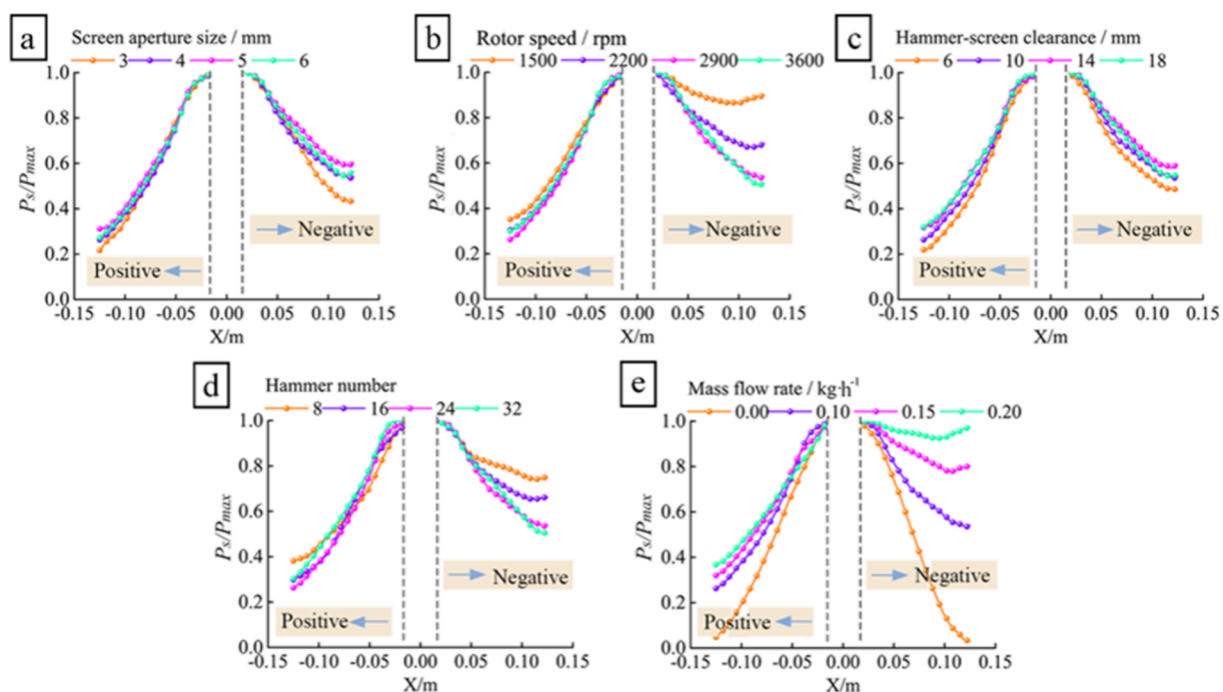
Figure 7. Variation of normalized static pressure with various factors in Region I. (a) Screen aperture size (b) Rotor speed (c) Hammer-screen clearance (d) Hammer number (e) Mass flow rate

Table 3. ANOVA of the Normalized Static Pressure

| Source	Positive region				Negative region			
	Sum of Squares	F-value	P-value	Coefficient Estimate	Sum of Squares	F-value	P-value	Coefficient Estimate
Linear Model	8.26	18.32	<0.01	–	75.06	40.77	<0.01	–
Screen aperture size	0.14	1.56	0.23	−0.23	0.51	1.40	0.26	−0.44
Rotor speed	0.85	9.53	<0.01	0.58	14.30	38.83	<0.01	2.36
Hammer-screen clearance	0.53	5.89	0.03	−0.45	0.05	0.13	0.73	−0.13
Hammer number	0.33	3.63	0.07	0.36	6.63	18.00	<0.01	1.61
Mass flow rate	6.77	74.79	<0.01	−1.74	56.05	152.21	<0.01	−5.01
Residual	1.26				5.16			
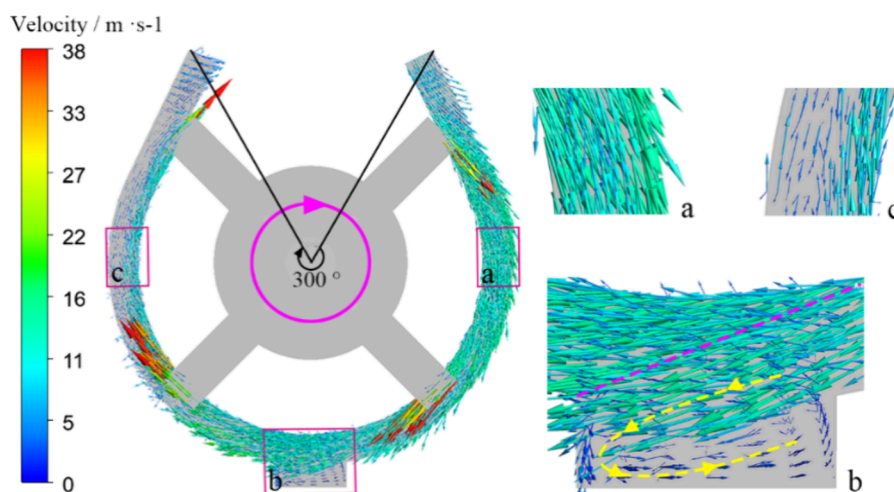
Figure 8. Velocity vector in Region II. (a) The right region. (b) The bottom region. (c) The left region.

and 7e). The static pressure gradient increased as the rotor speed and hammer number increased (Figures 7b, and 7d).

To quantitatively analyze the influence of various factors on the distribution of static pressure gradient, the slope of the fitting line of the static pressure normalization results of the airflow field in the positive and negative regions was used as the response value, and the significance of the influence of factors on the response values was explored. The linear model in Design-Expert was applied for the analysis of variance (ANOVA), and the results are listed in Table 3. The linear model was extremely
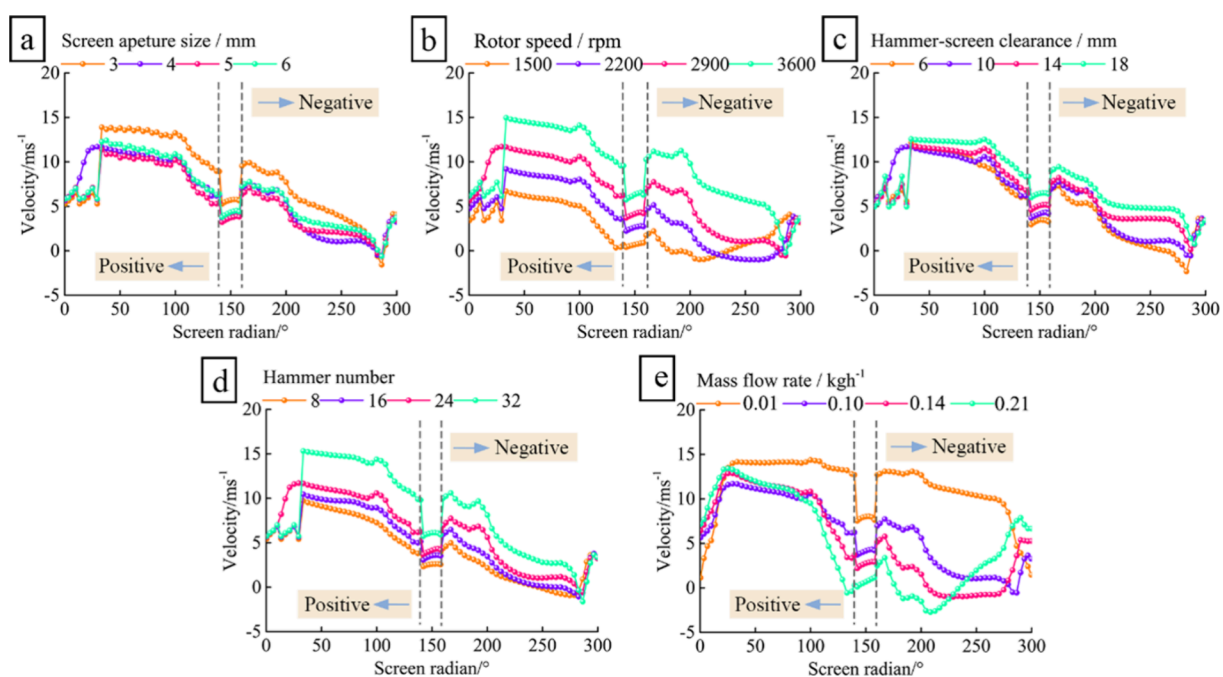
Figure 9. Influence of various factors on the fluid velocity in Region II. (a) Screen aperture size. (b) Rotor speed. (c) Hammer-screen clearance. (d) Hammer number. (e) Mass flow rate.

significant ($P < 0.01$), indicating that the ANOVA was reliable. The mass flow rate, rotor speed, and hammer number had a significant impact on the static pressure gradient distribution, respectively. And, the static pressure gradient was negatively correlated with mass flow rate but positively correlated with rotor speed and hammer number. The static pressure gradient was negatively correlated with screen aperture size, but it had no significant effect on the static pressure gradient distribution. However, the static pressure gradient was also negatively correlated with the hammer-screen clearance, but it had a significant effect on the static pressure gradient in the positive region and had no significant effect on the negative region. Reducing the rotor speed and hammer number, increasing the screen aperture size, the hammer-screen clearance, and the mass flow rate could decrease the static pressure gradient, so that both the static pressure gradient force pointing to the center of the rotor and the residence time were decreased to improve the screening efficiency and the crushing efficiency.

4.3. Velocity Distribution in Region II. The width of the circulation layer in the crushing chamber was set to 2 times the hammer screen clearance to study the airflow velocity in Region II. The airflow velocity vector diagram in the crushing inner circulation layer is shown in Figure 8.

The circulation movement near the screen was gradually formed by the fluid in the crushing chamber. The airflow entered the crushing chamber under the fan effect of the rotor and mass flow rate, which caused the gradual formation of the circulation movement near the screen. The airflow in the circulation layer moved tangentially along the screen surface as a whole, and the direction of airflow movement was the same except near the hammer area (Figure 8a). The ruminant trough had the effect of slowing down the airflow velocity of the circulation layer because part of airflow from the circulation layer generated an eddy on the ruminant trough, which reduced the airflow velocity (Figure 8b). After passing through the ruminant trough, part of the airflow flowed along the screen in the opposite direction in the rotor's rotational direction, which was primarily caused by the

impact of mass flow rate (Figure 8c). Airflow entering the crushing chamber continued to flow out of the screen aperture along the negative area near the screen surface, and the larger the mass flow rate, the more obvious reverse flow of airflow. Due to the acceleration effect of the high-rotation hammer on the airflow, the maximum airflow velocity in the circulation layer appeared at the tip of the hammer, which was about 83.46% of the linear velocity at the tip of the hammer.

The tangential average airflow velocity in the circulation layer was used to quantitatively analyze the influence of various factors on the airflow velocity in Region II shown in Figure 9. The airflow velocity of the circulation layer reduced as the screen aperture and mass flow rate increased (Figure 9a and Figure 9e). When the increase of screen aperture and mass flow rate, the normal airflow velocity through the screen aperture increased, and tangential airflow velocity decreased. The airflow velocity in the negative region of the rotor rotation increased when the mass flow rate was 0.21 kg/h (Figure 9e). It was because the excessive mass flow rate not only destroyed the movement of the circulation layer but also formed a circulation layer with reverse high-speed movement, which led to accelerating in the reverse region of the rotor rotation. The airflow velocity increased as the rotor speed, the hammer-screen clearance, and the hammer number increased (Figure 9b, Figure 9c, and Figure 9d). The increase in rotor speed and hammer number enhanced the fan effect of the rotor, which led to the increase of the airflow velocity in the crushing chamber and circulation layer. The wider the width of the circulation layer, the greater the proportion of the airflow accelerated by the hammer in the circulation layer, increasing the airflow velocity in the circulation layer. The airflow velocity in the circulation layer of the ruminant trough area was significantly lower, indicating that the ruminant trough had the effect of decelerating the airflow velocity in the circulation layer and crushing the indoor circulation layer (Figure 9).

To determine the significance of the influence of various factors on the airflow velocity in the circulation layer, the linear

model in Design-Expert was used for the ANOVA shown in Table 4. The linear model was extremely significant ($P < 0.01$),

Table 4. ANOVA of Velocity in the Circulation Layer

	Sum of Squares	F-value	P-value	Coefficient Estimate
Linear Model	59.39	22.51	<0.01	–
Screen aperture size	1.13	2.14	0.14	−0.66
Rotor speed	27.67	52.44	<0.01	3.28
Hammer-screen clearance	1.92	3.64	0.58	0.86
Hammer number	10.90	20.65	<0.01	2.06
Mass flow rate	19.52	36.99	<0.01	−2.95
Residual	7.39			

indicating the reliability of the results. The velocity of the circulation layer was significantly influenced by mass flow rate, rotor speed, and hammer number. Both rotor speed and hammer number had a positive correlation with the velocity of the circulation layer, however, the mass flow rate had a negative correlation. The velocity of the circulation layer was positively correlated with hammer-screen clearance and negatively correlated with the screen aperture size. However, they had no significant effects on the velocity. The relative velocity of the particles and the hammer decreased as the drag force on the particles increased with the velocity, which decreased the impact energy of the hammer on the particles and increased the energy loss of the hammer mill. Nevertheless, an extremely high particle velocity in the circulation layer prevented particle screening.[8,11] Combined with the results, the optimal circulation layer velocity could be obtained by changing the rotor speed, hammer number, and mass flow rate, which could provide a basis for determining the ideal operating parameters of the hammer mill.

4.4. Airflow Distribution in Region III. *4.4.1. Velocity Distribution of Airflow Field in Screen Aperture.* Figure 10 shows the airflow streamline in the screen aperture. The flow was disarranged and created an eddy (Figure 10a). The fan effect of the rotor caused the airflow in the crushing chamber to create a circulating layer in the tangential direction of the screen. When the airflow moved through the screen aperture, the flow direction of the airflow changed sharply, the static pressure

imbalance (Figure 10b) and the airflow velocity difference (Figure 10c) were created on both sides of the screen aperture, and resulted in a new eddy, whose velocity of the center was low(Figure 10d). The eddy could form a flow-solid driving force on the particles in the screen aperture. On the one hand, the eddy may drive the particles from the top of the screen surface to the aperture and evacuate the screen aperture under the effect of the static pressure imbalance between the inside and outside of the screen aperture. On the other hand, the eddy in the screen aperture could reduce the effective evacuation area of the screen aperture and the efficiency of the particle sieving in the crushing chamber. Meanwhile, the reduction of the effective evacuation area led to the particle size being several times smaller than the aperture size.

The distribution characteristics of eddy in the screen aperture and the influence of various factors on it as shown in Figure 11. With the increase in screen aperture size, the eddy range was decreased, and the eddy center moved to the outside of the screen aperture along the axial position (Figure 11a). When the screen aperture size was 6 mm, there was no eddy in the screen aperture, indicating that the larger the screen aperture size, the more difficult to form an eddy. With the increase in the rotor speed and hammer number, the eddy range was increased and the rotation center of the eddy moved to the outside of the screen aperture along the axial position (Figure 11b and Figure 11d), indicating that the higher the rotor speed and the more the hammer number, the easier to form an eddy in the screen aperture. The formation of the eddy occurred in the screen aperture even when the hammer-screen clearance was altered (Figure 11c). So the hammer-screen clearance had little effect on the formation of the eddy. With the increase in the mass flow rate, the range of the eddy in the screen aperture decreased. When the mass flow rate was 0.21 kg/h, there was no eddy in the screen aperture, indicating that the mass flow rate could effectively destroy the formation of an eddy in the screen aperture. This was mainly because the suction air could significantly reduce the airflow velocity of the circulating layer and increase the angle θ between the surface of the screen aperture and the airflow movement of the circulating layer, which was beneficial for the airflow in the circulating layer out of the screen aperture and reduced the velocity difference between
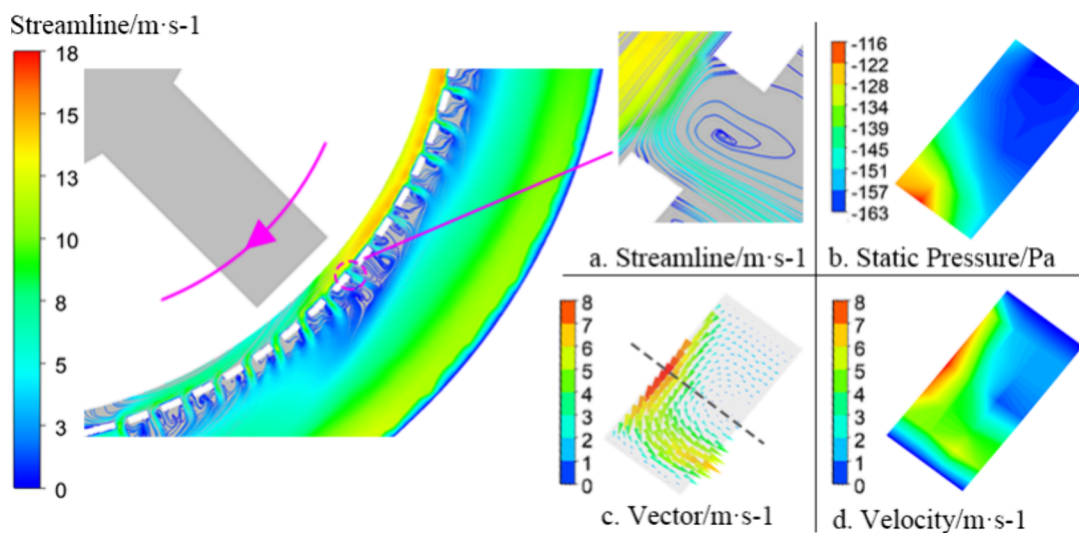

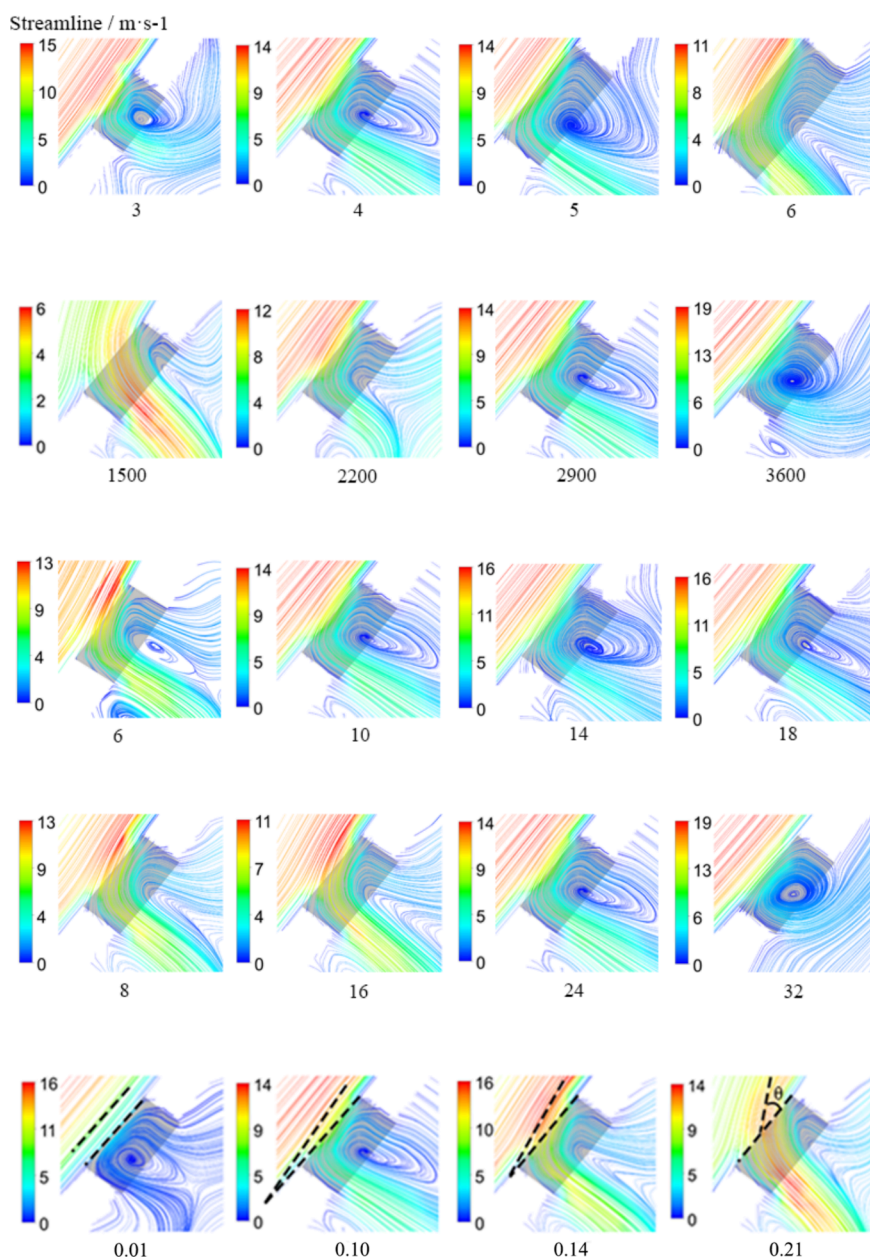**Figure 10.** Airflow streamlines in the screen aperture.

Figure 11. Influence of various factors on the eddy of screen apertures. (a) Screen aperture size. (b) Rotor speed. (c) Hammer-screen clearance. (d) Hammer number. (e) Mass flow rate.

the two sides of the screen. Therefore, it was difficult to form an eddy when the airflow through the screen aperture with a large amount of mass flow rate.

4.4.2. Pressure Imbalance Inside and Outside the Screen Aperture. The static pressure distribution inside and outside the screen aperture is shown in Figure 12. The static pressure on the inside surface of the screen was higher than that on the outside surface, indicating that there was a static pressure imbalance inside and outside the screen, which was beneficial for the evacuation of particles from the screen during the crushing process. The airflow in the circulation layer could be divided into three parts from the velocity vector in Figure 12, part of the airflow directly flew out of the crushing chamber through the screen aperture (I); part of the airflow continued to circulate along the tangential direction of the inside surface of the screen (III); and part of the airflow impacted with the inside surface of the screen mesh and screen aperture at a high speed, and the

static pressure of the airflow in the impact area was large, resulting in the static pressure of the inside surface of the screen aperture higher than that of the outside (II). Also, the static pressure of the airflow field in the positive screen (front end of the ruminate tank) was higher than that in the negative screen (back end of the ruminate tank) shown in Figure 12.

The static pressure distribution of the airflow field inside and outside the screen aperture could be qualitatively analyzed in Figure 12, and it was necessary to apply the numerical simulation for quantitative analysis. The wrap angle of the screen was 300°, and the angles between the reference line and the center line of the four hammers were 15°, 105°, 195°, and 285°, respectively (Figure 12). The influence of various factors on the static pressure imbalance is shown in Figure 13. The static pressure imbalance inside and outside of the positive screen was higher than that of the negative screen. At the left and right ends of the curves, there were peaks at the x-coordinates of 15°, 105°, and
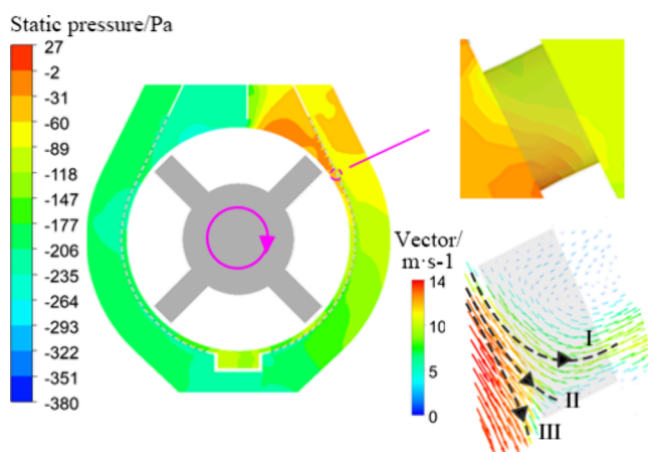
Figure 12. Inside and outside static pressure contour for screen apertures.

195°. For the above three points, the peak on the left (the back of the hammer) of each coordinate point was its minimum, and the peak on the right (the front of the hammer) was the maximum. This shows that the static pressure inside and outside the screen aperture close to the hammer changed greatly, indicating that the static pressure imbalance at the back end of the hammer was small, and in the opposite direction was large. However, when the x-coordinate was 285°, the static pressure imbalance did not have the above distribution characteristics, which was mainly because the outside airflow near the position was sucked into the crushing chamber (Figure 13f), resulting in a small static pressure imbalance in the screen aperture and a negative static pressure imbalance. With the increase in the screen diameter, the static pressure imbalance decreased (Figure 13a). However, with the increase in rotor speed, hammer number, and mass flow rate, the static pressure imbalance increased (Figure 13b, Figure

13d, and Figure 13e). The change of hammer-screen clearance had no obvious effect on the static pressure imbalance (Figure 13c).

To determine the significance of the influence of various factors on the static pressure imbalance inside and outside the screen aperture, the linear model in Design-Expert was used for the ANOVA shown in Table 5. The linear model was extremely significant ($P < 0.01$), indicating the reliability of the results of ANOVA. The mass flow rate, rotor speed, and screen aperture size had significant effects on the static pressure imbalance. The static pressure imbalance was positively correlated with the mass flow rate and rotor speed but negatively correlated with the screen aperture size. With the increase in mass flow rate, the static pressure imbalance increased. However, the excessive static pressure imbalance may lead to the adsorption of large particles on the inside of the screen aperture to reduce the effective area of the screen mesh, which not only reduces the impacting efficiency of the material particles and the hammer but also reduces the material evacuation efficiency, resulting in the reduction in the crushing efficiency of the hammer mill. The results were consistent with Qin et al., that with the increase in mass flow rate, the unit energy consumption of the hammer mill increased then decreased.[38] The static pressure imbalance was positively correlated with hammer screen clearance, but hammer screen clearance had no significant effect on static pressure imbalance. The hammer number had a significant effect on the static pressure imbalance of the positive screen aperture of the rotor in the crushing chamber and had no significant effect on the negative region.

5. CONCLUSIONS

In this study, CFD was used to study the airflow distribution characteristics in the crushing chamber of the hammer mill. Compared with the pressure drop between the inlet and outlet of the experiment and the numerical simulation, the CFD model
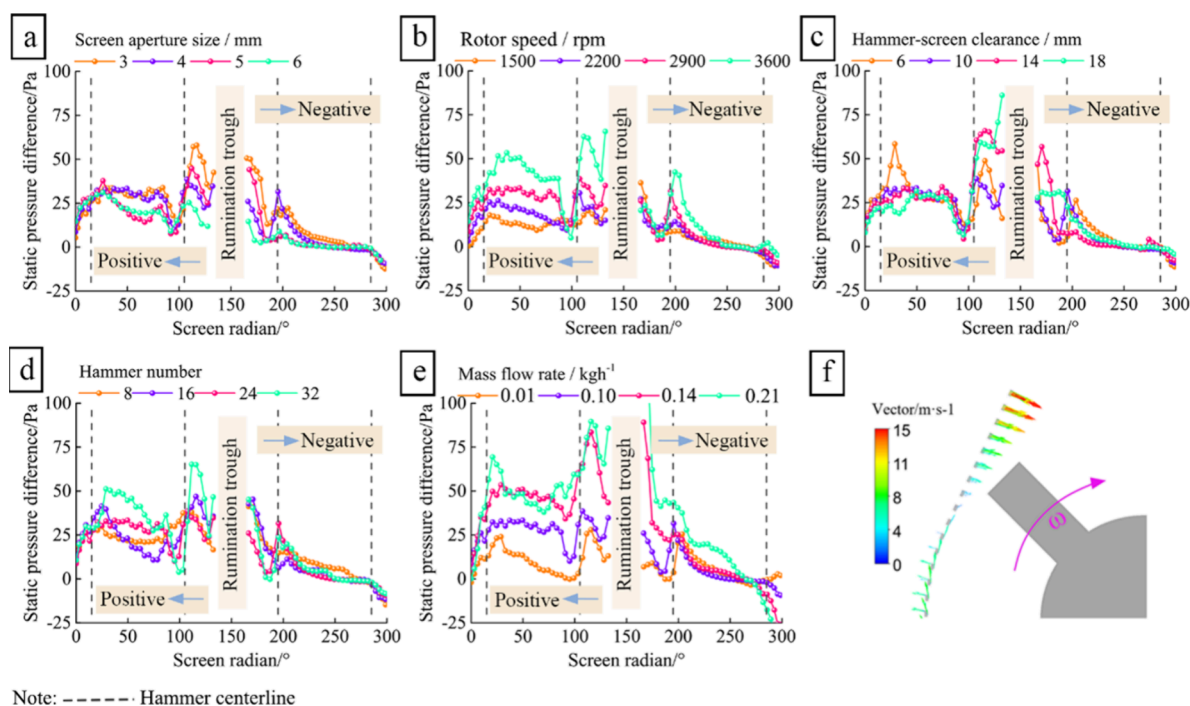

Note: ----- Hammer centerline

Figure 13. Influence of various factors on the static pressure imbalance inside and outside the screen aperture. (a) Screen aperture size. (b) Rotor speed. (c) Hammer-screen clearance. (d) Hammer number. (e) Mass flow rate. (f) When the x-coordinate was 285°, the distribution of static pressure.

Table 5. ANOVA of the Static Pressure Imbalance Inside and Outside the Screen Aperture

Source	Positive screen				Negative screen			
	Sum of Squares	F-value	P-value	Coefficient Estimate	Sum of Squares	F-value	P-value	Coefficient Estimate
Linear Model	1700.31	41.84	<0.01	−	133.39	8.47	<0.01	−
Screen aperture size	85.05	10.46	<0.01	−5.76	40.48	12.85	<0.01	−3.97
Rotor speed	474.18	58.34	<0.01	13.59	19.64	6.24	0.03	2.77
Hammer-screen clearance	3.12	0.38	0.55	1.10	4.30	1.36	0.26	1.29
Hammer number	47.27	5.82	0.03	4.29	3.19	1.01	0.33	−1.12
Mass flow rate	1078.31	132.67	<0.01	21.96	63.24	20.08	<0.01	5.32
Residual	113.79				44.09			

was validated. The influence of the screen aperture size, rotor speed, hammer number, hammer-screen clearance, and mass flow rate on the airflow distribution in three regions was studied. In the rotor diameter range of the hammer mill, the static pressure of the airflow was relatively uniformly distributed along the axial direction, and gradient distributed along the radial direction. The increase in the rotor speed significantly improved the distribution of the radial static pressure gradient of the airflow ($P < 0.05$), and the increase in the mass flow rate significantly reduced the distribution of the radial static pressure gradient of the airflow ($P < 0.05$). In the circulation layer of the hammer mill, the maximum airflow velocity was about 83.46% of the linear velocity at the end of the hammer. The increase in the rotor speed and hammer number significantly increased the circulation layer airflow velocity ($P < 0.05$), and the increase in the mass flow rate significantly reduced the airflow velocity ($P < 0.05$). When the airflow was through the screen aperture, the static pressure imbalance and the airflow velocity difference were formed on the inside and outside of the screen aperture, which led to the eddy of the screen aperture, and the velocity of the eddy center was low. With an increase in rotor speed and hammer number, it was more likely to form an eddy in the screen aperture. It was difficult to form eddy in the large screen aperture size ($\varphi = 6.0$ mm). The increase in the mass flow rate was beneficial to destroy the eddy formed in the screen aperture. The static pressure of the airflow in the crushing chamber on the inside surface of the screen aperture was higher than that on the outside surface, so there was a static pressure imbalance between the inside and outside of the screen aperture. The increase in mass flow rate and rotor speed increased significantly the static pressure imbalance ($P < 0.05$), and the increase in screen aperture size decreased significantly the static pressure imbalance ($P < 0.01$).

This study revealed the distribution characteristics of the airflow field in the hammer mill and explored the influence of various factors on the distribution of the airflow field in three regions in the crushing chamber. However, it is still necessary to quantitatively analyze the eddy intensity of the airflow in the screen aperture, and the significance of the influence of each factor on the eddy intensity in the screen aperture is further analyzed.

AUTHOR INFORMATION

Corresponding Author

Zhiyou Niu − *College of Engineering, Huazhong Agricultural University, Wuhan 430070, China; Key Laboratory of Smart Farming for Agricultural Animals, Ministry of Agriculture, Wuhan 430070, China;* Email: nzhy@mail.hzau.edu.cn

Authors

Hongcheng Li − *Ocean Mechanical and Electrical College, Xiamen Ocean Vocational College, Xiamen 361100, China*

Shanchen Jiang − *College of Engineering, Huazhong Agricultural University, Wuhan 430070, China; Key Laboratory of Smart Farming for Agricultural Animals, Ministry of Agriculture, Wuhan 430070, China*

Rong Zeng − *College of Engineering, Huazhong Agricultural University, Wuhan 430070, China; Key Laboratory of Smart Farming for Agricultural Animals, Ministry of Agriculture, Wuhan 430070, China*

Jie Geng − *College of Engineering, Huazhong Agricultural University, Wuhan 430070, China; Key Laboratory of Smart Farming for Agricultural Animals, Ministry of Agriculture, Wuhan 430070, China;* orcid.org/0000-0003-1372-6807

Complete contact information is available at:
https://pubs.acs.org/10.1021/acsomega.4c02187

Author Contributions

Hongcheng Li: Conceptualization, Methodology, Software, Resources, Writing—original draft. **Shanchen Jiang:** Methodology, Software, Writing—original draft. **Rong Zeng:** Methodology, Investigation, Validation, Writing—review and editing. **Jie Geng:** Resources, Data curation, Visualization, Writing—review and editing. **Zhiyou Niu:** Supervision, Project administration, Funding acquisition, Writing—review and editing.

Notes

The authors declare no competing financial interest.

REFERENCES

(1) Lyu, F.; Thomas, M.; Hendriks, W. H.; van der Poel, A. F. B. Size reduction in feed technology and methods for determining, expressing and predicting particle size: A review. *Anim. Feed Sci. Technol.* **2020**, *261*, 114347.

(2) Ghorbani, Z.; Masoumi, A. A.; Hemmat, A. Specific energy consumption for reducing the size of alfalfa chops using a hammer mill. *Biosystems Engineering* **2010**, *105*, 34−40.

(3) Liermann, W.; Berk, A.; Hüther, L.; Böschen, V.; Dänicke, S. Fine grinding or expanding of feed as pre-treatment for pelleting in dependence on dietary rapeseed expeller proportion: Nutritional consequences for broilers. *Arch. Anim. Nutr.* **2019**, *73*, 239−254.

(4) Sudha, L.; Dillibabu, R.; Srivatsa Srinivas, S.; Annamalai, A. Optimization of process parameters in feed manufacturing using Artificial neural network. *Comput. Electron. Agric.* **2016**, *120*, 1−6.

(5) Al-Rabadi, G. J. The effect of hammer mill screen size on processing parameters and starch enrichment in milled barley. *Jordan J. Agric. Sci.* **2013**, *9*, 162.

(6) Thomas, M.; Hendriks, W. H.; van der Poel, A. F. B. Size distribution analysis of wheat, maize and soybeans and energy efficiency using different methods for coarse grinding. *Animal Feed Science and Technology* **2018**, *240*, 11−21.

(7) Guo, L.; Tabil, L. G.; Wang, D.; Wang, G. Influence of moisture content and hammer mill screen size on the physical quality of barley, oat, canola and wheat straw briquettes. *Biomass and Bioenergy* **2016**, *94*, 201−208.

(8) Liu, C.; Zhao, X. The influence of air intake volume on efficience of hammer mill. *Trans. Chin. Soc. Agric. Mach.* **1991**, 56−62.

(9) Tian, H.; et al. Design of combination sieve for hammer feed mill to improve crushing performance. *Trans. Chin. Soc. Agric. Eng.* **2018**, *34*, 45−52.

(10) He, Y. An analysis on the relationship between the characteristics and parameters of hammer mills. *Trans. Chin. Soc. Agric. Eng.* **1988**, 54−62.

(11) Liu, C.; Zhao, X. Characteristics of gaseous-solid phase circualtion layer of hammer mill and the mechanism of its influence on crushing-screening process. *Trans. Chin. Soc. Agric. Mach.* **1991**, 36−43.

(12) Wang, J.; Zhang, G.; Cao, L. Research of materials motion law in separation flow of new type hammer feed grinder. *Trans. Chin. Soc. Agric. Eng.* **2013**, *29*, 18−23.

(13) Ghodki, B. M.; Charith Kumar, K.; Goswami, T. K. Modeling breakage and motion of black pepper seeds in cryogenic mill. *Advanced Powder Technology* **2018**, *29*, 1055−1071.

(14) Metzger, M. J.; Glasser, B. J. Numerical investigation of the breakage of bonded agglomerates during impact. *Powder Technol.* **2012**, *217*, 304−314.

(15) Wang, Y.; Yu, X.; Yu, z. Line speed difference between material and hammer, and material's screen passing ability determine hammer-mill's grinding effect. *Feed Industry* **2016**, *37*, 1−9.

(16) Cao, K.; Hao, B. *Modern China Feed Engineering*; Shanghai Scientific and Technologyical Literature Press, 2014.

(17) Takeuchi, H.; Nakamura, H.; Iwasaki, T.; Watano, S. Numerical modeling of fluid and particle behaviors in impact pulverizer. *Powder Technol.* **2012**, *217*, 148−156.

(18) Liu, F.; Wang, W.; Zhang, T.; Ma, Q.; Zhan, M. Air flow field numerical simulation and test of hammer rubbing machine. *Trans. Chin. Soc. Agric. Mech* **2018**, *49*, 227−232.

(19) Budăcan, I.; Deac, I. Numerical modeling of CFD model applied to a hammer mill. *Bull. Univ. Agric. Sci. Vet. Med. Cluj-Napoca. Agric.* **2013**, *70*, 273−282.

(20) Koeninger, B.; Hensler, T.; Romeis, S.; Peukert, W.; Wirth, K.-E. Dynamics of fine grinding in a fluidized bed opposed jet mill. *Powder Technol.* **2018**, *327*, 346−357.

(21) Cao, L.; Shi, X.; Wang, J.; Bai, Y. Design and experiment of separation device of hammer feed mill. *Trans. Chin. Soc. Agric. Mach.* **2016**, *47*, 128−133.

(22) Pei, Y. *Simulation and Analyzation on Flow Field in Crashing Cavity of New-Type Feed Hammer Mill*; Inner Mongolia University of Science & Technology, 2014.

(23) Zhou, Y.; Guo, T. *Advanced Fluid Mechanics*; China Electric Power Press, 2008.

(24) Nakamura, H.; Kan, H.; Takeuchi, H.; Watano, S. Effect of stator geometry of impact pulverizer on its grinding performance. *Chem. Eng. Sci.* **2015**, *122*, 565−572.

(25) Shah, K. V.; Vuthaluru, R.; Vuthaluru, H. B. CFD based investigations into optimization of coal pulveriser performance: Effect of classifier vane settings. *Fuel Process. Technol.* **2009**, *90*, 1135−1141.

(26) Shih, T.-H.; Liou, W. W.; Shabbir, A.; Yang, Z.; Zhu, J. A new k-ε eddy viscosity model for high Reynolds number turbulent flows: Model development and validation. *Comput. Fluids* **1995**, *24*, 227−238.

(27) Wang, X.; Xiong, A. *High Fluid Mechanics*, 1st ed.; Huazhong University of Science & Technology Press, 2003.

(28) Zeng, Y.; Zhang, S.; Zhou, Y.; Li, M. Numerical simulation of a flow field in a turbo air classifier and optimization of the process parameters. *Processes* **2020**, *8*, 237.

(29) Toneva, P.; Epple, P.; Breuer, M.; Peukert, W.; Wirth, K.-E. Grinding in an air classifier mill - Part I: Characterisation of the one-phase flow. *Powder Technol.* **2011**, *211*, 19−27.

(30) Wang, J.; Wang, C.; Wang, F. Numerical simulation on three-dimensional turbulence air flow of 9R-40 rubbing and breaking machine based on Fluent software. *Trans. Chin. Soc. Agric. Eng.* **2010**, *26*, 165−169.

(31) Ma, Q.; Liu, F.; Zhao, M. Working mechanism and structure optimization of hammer of rubbing machine. *Trans. Chin. Soc. Agric. Eng.* **2016**, *32*, 7−15.

(32) Liying, C.; Chundong, L. *Second International Conference on Mechanic Automation and Control Engineering*, 2011.

(33) Wang, H.; Liu, Y. *ANSYS Fluent Fluid Numerical Calculation Method and Examples*; China Railway Publishing House Co., LTD., 2015.

(34) Ämmälä, A.; Pääkkönen, T. M.; Illikainen, M. Role of screen plate design in the performance of a rotor impact mill in fine grinding of biomass. *Industrial Crops and Products* **2018**, *122*, 384−391.

(35) Wang, Z.; Wu, P.; Cao, L. Simulation on air-solid two-phase flow in discharge pipe of a new-model hammer mill. *J. Inner Mongolia Agric. Univ.* **2009**, *30*, 184−187.

(36) Wang, H. *Fluid Mechanics as I Understand It*; National Defense Industry Press, 2014.

(37) Yang, K. *Crushing Device Optimization and Hydraulic System Design of Stalk Pulling Crushe*; Guizhou University, 2018.

(38) Qin, Y. *Studies on the Effects of Hammer Mill Performance on the Grinding Results of Normal Feedstuffs*; Jiang Nan University, 2009.